This is a repository copy of *Multi-scale approaches for the simulation of cardiac electrophysiology: I – sub-cellular and stochastic calcium dynamics from cell to organ*.

Version: Accepted Version

Article:

Multi-scale approaches for the simulation of cardiac electrophysiology: I - sub-cellular and stochastic calcium dynamics from cell to organ

Michael A. Colman[a,*], Maxx Holmes[a], Dominic G. Whittaker[a,b], Izzy Jayasinghe[a], Alan P. Benson[a]

[a]School of Biomedical Sciences University of Leeds, Leeds LS2 9JT, UK

[b]School of Mathematical Sciences, University of Nottingham, Nottingham NG7 2RD, UK

*Correspondence to m.a.colman@leeds.ac.uk (MAC)

Highlights

- Computational models of cardiac calcium handling are powerful tools to understand the complex mechanisms underlying physiological and pathophysiological phenomena.
- This article describes the fundamental equations describing calcium handling at the spatial, sub-cellular scale.
- And outlines two different discretisation approaches for practical simulation of spatio-temporal sub-cellular calcium dynamics.
- Finally, multi-scale integration methods for tissue-scale simulation of stochastic dynamics are described.

Abstract

Computational models of the heart at multiple spatial scales, from sub-cellular nanodomains to the whole-organ, are a powerful tool for the simulation of cardiac electrophysiology. Application of these models has provided remarkable insight into the normal and pathological functioning of the heart. In these two articles, we present methods for modelling cardiac electrophysiology at all of these spatial scales. In part one, presented here, we discuss methods and approaches for modelling sub-cellular calcium dynamics at the whole-cell and organ scales, valuable for modelling excitation-contraction coupling and mechanisms of arrhythmia triggers.

1. Intro

The periodic cycling of calcium (Ca^{2+}) ions controls excitation-contraction coupling (ECC) in cardiomyocytes, the mechanism by which electrical excitation triggers the development of mechanical force [1]. Intracellular Ca^{2+} homeostasis is relevant for maintaining appropriate cardiac performance required to meet the dynamic demands of the body, and has also been linked to pro-arrhythmogenic cellular phenomena [2,3]. Elucidation of the complex and multi-scale interactions which determine the mechanisms by which intracellular Ca^{2+} cycling underlies (patho)physiological function is therefore critical not only for fundamental

understanding of the electro-mechanical system of the heart, but also to the clinical motivations of treating and managing life-altering and -threatening cardiovascular disease [4,5].

The system maintaining Ca^{2+} homeostasis comprises multiple membrane transport channels and sub-cellular structures, the complex interactions of which are challenging to dissect with purely experimental approaches. Computational modelling has proved a powerful tool to supplement experimental studies and tease apart the mechanisms of cardiac function in health and disease [6,7]. However, developing accurate and realistic models of intracellular Ca^{2+} homeostasis presents a number of additional challenges compared to the point-source cell models traditionally used. Namely, one must attempt to simultaneously account for: (i) the co-localisation between channels at the nanometre scale; (ii) stochastic state transitions in restricted nanodomains; (iii) the spatial distribution of channels and membrane structures throughout the intracellular volume; and (iv) the interactions of heterogeneous cells in the syncytium of cardiac tissue. Over the last decade, multiple research groups have made significant advancements in the development of methodologies and approaches to address these challenges [8–20]; within this context, this article focuses on those developed by and utilised within our lab.

We will first discuss the primary components of the intracellular Ca^{2+} handling system and mechanisms of pro-arrhythmogenic phenomena to provide a context for the computational models. The methods described are focussed on two motivations: (i) modelling cellular spatial structure-function relationships underlying ECC and dysfunctional homeostasis, and (ii) multi-scale approaches for efficient modelling of Ca^{2+}-dependent spontaneous excitations in tissue. The computational models referred to are provided open-source and can be found in the lab's Github repository (https://github.com/michaelcolman/) and through the lab's website (http://physicsoftheheart.com/). This is part one of a two-part article; see Benson et al. in this issue for part two, which discusses methods for modelling structure-function relationships in cardiac tissues.

2. The intracellular Ca^{2+} handling system

At the whole-cell scale, Ca^{2+} homeostasis is regulated by the balance of multiple Ca^{2+} fluxes and depends on the process of Ca^{2+}-induced-Ca^{2+}-release (CICR; Figure 1A): During cellular excitation, the L-type-Ca^{2+}-channels (LTCCs) open and permit an influx of Ca^{2+} from the extracellular space; the elevated intracellular Ca^{2+} concentration promotes binding with the type-2 ryanodine receptors (RyRs), which release a larger amount of Ca^{2+} from the intracellular Ca^{2+} store (the sarcoplasmic reticulum; SR) into the bulk intracellular space. Homeostasis is maintained by effluxes through the membrane channels of the sodium-calcium exchanger (NCX) and the Ca^{2+} ATPase pump, which remove Ca^{2+} into the extracellular space, and the SR-Ca^{2+}-pump (SERCA), which refills the SR.

The distributed spatial structure of the sarcolemmal and SR membranes and their associated channel proteins facilitates uniform cellular contraction, but also has potentially pro-arrhythmogenic implications. CICR occurs in restricted nanodomains called dyads, which co-localise the LTCCs and RyRs; each dyad contains only a few LTCC and RyR channels (typically 5-15 and 5-200, respectively [21]) within a very small volume ($O(10^{-3})$ μm^3) where random state transitions can have important implications. Dyads are distributed throughout the intracellular volume and are functionally coupled by Ca^{2+} diffusion, supporting robust whole-cell triggered Ca^{2+} release which, in normal conditions, can normalise the stochastically-driven variability of triggered Ca^{2+} sparks occurring in individual dyads. However, this functional coupling in combination with inter-dyad heterogeneity has been shown to be a critical factor underlying the dynamics of Ca^{2+}-transient alternans [8,22], referring to beat-to-beat alternations to the magnitude of the Ca^{2+} transient and developed force which can both directly

1 impact cardiac output as well as lead to arrhythmia. Moreover, random openings of single or
2 few RyRs can raise the local Ca^{2+} concentration sufficiently to trigger further openings within
3 the dyad, potentially leading to a whole-dyad event: the spontaneous Ca^{2+} spark. Spatial-diffuse
4 coupling amplifies this intrinsic feedback mechanism and provides a dynamical substrate for
5 the propagation of microscopic fluctuations to the macroscopic scale (whole-cell) as a spark-
6 induced-spark mediated Ca^{2+} wave (Figure 1B). Activation of NCX as this wave propagates
7 throughout the intracellular volume results in a transient inward current that can depolarise the
8 cell membrane as a delayed-after-depolarisation (DAD) or full triggered action potentials (TA;
9 Figure 1B), potentially triggering spontaneous focal excitations and arrhythmia in tissue. Thus,
10 stochastic dynamics in sub-cellular Ca^{2+} handling can have implications on whole-cell and
11 whole-organ function; accounting for these microscopic features in efficient cell models is one
12 major challenge faced by the community.

13 The methods described in this article aim to build multi-scale modelling approaches to
14 accurately simulate these underlying heterogeneous sub-cellular spatial-dynamics and their
15 impact on tissue function.

16 3. Methods for modelling sub-cellular spatial Ca^{2+} dynamics

17 This section describes methods for modelling the structure-function relationships of
18 intracellular Ca^{2+} handling at two different levels of detail, corresponding to different
19 discretisation approaches. The first (Figure 2A), at the coarsest resolution, approximates a cell
20 as a 3D grid of "calcium-release-units" (CRUs) [8,23] which are comprised of multiple
21 intracellular and SR compartments, and are thus referred to herein as **compartmentalised**
22 models. The second (Figure 2B), higher resolution approach discretises the intracellular spaces
23 as volumes within which free diffusion occurs [9,12,20], and are thus herein referred to as **free-**
24 **diffusion** models. The two models operate at discretisation scales of $O(10^0)$ μm^3 and $O(10^2)$
25 nm^3, respectively, and present different advantages: namely, the ability to directly study
26 structure-function relationships at the super resolution scale (free-diffusion models), and the
27 ability to carry out high-throughput simulations suitable for statistical analysis
28 (compartmentalised models). The fundamental schematic structure and governing equations of
29 the models are the same, described in the next section. Instructions and worked examples for
30 implementing both of these model types using the source-code developed in the lab is provided
31 in the Supplementary Material S1 – Worked Examples and the extensive documentations
32 provided with the code.

33 3.1. Fundamental model setup

34 Whereas some of the fine details may differ, the fundamental structure of whole-cell spatio-
35 temporal models of intracellular Ca^{2+} handling in the literature in-general comprises five
36 compartments (Figure 2Aiii, Biii): the intracellular space is split into the compartments of the
37 dyadic cleft, the local sub-space, and the bulk intracellular space; the SR is split into the
38 network and junctional compartments (nSR and jSR, respectively). The dyadic cleft can be
39 treated as a single compartment with volume v_{ds} and associated numbers of LTCCs and RyRs
40 (these parameters can vary between individual dyads); the bulk intracellular space, network SR
41 space and (optionally) the sub-space can be spatially coupled to their neighbours, whereas the
42 junctional SR and dyad compartments are spatially isolated. Ca^{2+} dynamics in each of these
43 five compartments is described by the general homeostatic equations:

$$44 \qquad \frac{d[Ca^{2+}]_{cyto}}{dt} = \beta_{cyto}\left(\mathbf{D}\nabla^2[Ca^{2+}]_{cyto} + \phi_{cyto} + \left(v_{ss}/v_{cyto}\right)J_{ss}\right) \qquad (1)$$

1
$$\frac{d[Ca^{2+}]_{SS}}{dt} = \beta_{SS} \left(\mathbf{D}\nabla^2 [Ca^{2+}]_{SS} + \phi_{SS} - J_{ss} + \left(v_{ds}/v_{ss} \right) J_{ds} \right) \tag{2}$$

2
$$\frac{d[Ca^{2+}]_{nSR}}{dt} = \beta_{nSR} \left(\mathbf{D}\nabla^2 [Ca^{2+}]_{nSR} + \phi_{nSR} - \left(v_{jsr}/v_{nsr} \right) J_{jSR} \right) \tag{3}$$

3
$$\frac{d\left[Ca^{2+}\right]_{ds}}{dt} = \phi_{ds} - J_{ds} \tag{4}$$

4
$$\frac{d\left[Ca^{2+}\right]_{JSR}}{dt} = \beta_{jSR} \left(\phi_{JSR} + J_{jSR} \right) \tag{5}$$

5
Where transfer between compartments is given by:

6
$$J_{ss} = \left(\left[Ca^{2+} \right]_{SS} - \left[Ca^{2+} \right]_{cyto} \right) \tau_{ss}^{-1} \tag{6}$$

7
$$J_{ds} = \left(\left[Ca^{2+} \right]_{ds} - \left[Ca^{2+} \right]_{SS} \right) \tau_{ds}^{-1} \tag{7}$$

8
$$J_{jSR} = \left(\left[Ca^{2+} \right]_{nSR} - \left[Ca^{2+} \right]_{jSR} \right) \tau_{jSR}^{-1} \tag{8}$$

9
And the general form for reaction terms are:

10
$$\phi_{cyto} = J_{NaCa} + J_{pCa} + J_{Cab} - \left(J_{up} - J_{leak} \right) - J_{trpn} \tag{9}$$

11
$$\phi_{nSR} = \left(J_{up} - J_{leak} \right) \left(v_i/v_{nsr} \right) \tag{10}$$

12
$$\phi_{ss} = J_{NaCa\_SS} + J_{pCa\_SS} + J_{Cab\_SS} \tag{11}$$

13
$$\phi_{ds} = J_{rel} + J_{CaL} \tag{12}$$

14
$$\phi_{JSR} = -J_{rel} \left(v_{ds}/v_{jSR} \right) \tag{13}$$

15 Where ∇^2 is the spatial Laplacian operator in 3D, β refers to instantaneous buffering, v refers
16 to the volumes of the compartments and τ to the time-constants of diffusion. Full equations
17 and parameters are given in the Supplementary Material S2 – Model description, and in
18 associated publications [11–13].

19 3.2. Discretisation scheme: compartmentalised models

20 Following the approach outlined in [8,10,23], a coarse-grained and efficient discretisation of
21 the whole-cell can be attained by considering the volumes of each compartment associated with
22 each dyad as a single CRU (Figure 2A), corresponding to discretisation in the range 1-2 µm.
23 Such models assume homogeneous distances between dyads (transverse-longitudinal
24 anisotropy can still be included) but have proved valuable in mechanistic investigation of Ca^{2+}-
25 diffusion dependent phenomena. Each CRU contains a single volume for each of the five
26 compartments and contains a flux from each reaction term. Spatial coupling for the cytoplasm,

1 sub-space and network SR can be approximated by coupling the relevant compartment of each
2 CRU to its six nearest neighbours in each of the principal directions and defining a time-
3 constant of diffusion between them; time-constants can differ between types of compartment,
4 and in the transverse and longitudinal directions to introduce anisotropy. Thus, the diffusion
5 terms in equations 1-3 can be approximated with the following discretisation:

6
$$\mathbf{D}\nabla^2[Ca^{2+}]_{x=cyto,SS,nSR} \approx J_{Ca\_diff\_x} = \sum_{i=1}^{i=3}\left(\frac{{}^{e_i+1}[Ca^{2+}]_x + {}^{e_i-1}[Ca^{2+}]_x - 2{}^{e_i}[Ca^{2+}]_x}{\tau_{x,e_i}}\right) \quad (14)$$

7 Where example [11,13] values for the time constants, relative to the longitudinal axis of the
8 cell, are $2.9_{\parallel}$ and $2.3_{\perp}$ ms (cytoplasm), $12_{\parallel}$ and $7_{\perp}$ ms (network SR), and $2.2_{\parallel}$ and $1.35_{\perp}$ ms
9 (sub-space). Every other equation is discretised by solving it locally for each CRU, n (= 1, 2
10 … N_{CRUs}). Different cellular geometries can be specified by defining different extents of the
11 CRU grid in each direction, representing, for example a typical ventricular cell ($15 \times 20 \times 65$
12 $\approx 15 \times 20 \times 100$ μm^3) or with adjusted parameters to reproduce variability, remodelling or
13 similar. Note that distances in this type of model are not explicitly defined, but are rather
14 captured in the time constants of diffusion. Please see [8] for estimating time-constants based
15 on distance and local buffering. These models are available in the "**Multi-scale cardiac
16 simulation framework (MSCSF)**" repository on the lab's Github.

17 3.3. Discretisation scheme: free-diffusion models

18 Following the earlier works of Li et al. 2010 [9] and Nivala et al. 2012 [20], an approach was
19 developed in Colman et al. 2017 [12] to integrate multiple reconstructed cellular structures into
20 free-diffusion models of spatio-temporal calcium handling (Figure 2B). Fundamental model
21 setup is similar to those studies, with the addition of mapping functions to describe the
22 heterogeneous structures of the SR and T-system. This approach discretises the space
23 explicitly, rather than through compartmentalisation of CRUs. An idealised model is first
24 created by selecting a volume to correspond to the intracellular space – either a cuboid or a
25 cylinder with dimensions that match those of cardiac cells (10-20 μm × 10-20 μm × 50-150
26 μm). This volume can be discretised at a chosen resolution in the range $\Delta x = 100 – 250$ nm and
27 the diffusion terms in equations 1-3 are modelled by the isotropic, 6-node finite difference
28 approximation:

29
$$\mathbf{D}\nabla^2[Ca^{2+}]_{x=cyto,SS,nSR} \approx \sum_{i=1}^{i=3}\mathbf{D}\left(\frac{{}^{e_i+1}[Ca^{2+}]_x + {}^{e_i-1}[Ca^{2+}]_x - 2{}^{e_i}[Ca^{2+}]_x}{\Delta x_{e_i}^2}\right) \quad (15)$$

30 3.3.1. Model setup

31 The model can be considered to be tri-domain, wherein each voxel of the intracellular space
32 comprises domains corresponding to the bulk intracellular space, the network SR space, and
33 the sub-space (Figure 2B). Individual voxels can be selected to correspond to the locations of
34 the dyads, and therefore also contain a dyad and junctional SR compartment (which are coupled
35 to the sub-space and network SR compartments of that voxel, respectively). Mapping functions
36 must therefore be created to relate dyad m *(m = 1, 2 ... M)* with voxel n *(n = 1, 2 ... N)*, where
37 M and N are the total numbers of dyads and voxels in the model, respectively. These functions
38 are defined as $\theta_{dyad}(m) = n$ and inverse function $\theta_{dyad}^{-1}(n) = m$. Following this discretisation,
39 the model equations must be updated to give:

1
$$^{n}J_{ds} = \left(\begin{array}{c} ^{\theta_{dyad}^{-1}(n)=m}\left[Ca^{2+}\right]_{ds} - {}^{n}\left[Ca^{2+}\right]_{SS} \end{array} \right)\tau_{ds}^{-1} \left. \begin{array}{c} \forall n \in \theta_{dyad}(m) \\ \\ \forall n \notin \theta_{dyad}(m) \end{array} \right\} \qquad (16)$$

2
$$^{n}J_{jSR} = \left(\begin{array}{c} ^{\theta_{dyad}^{-1}(n)=m}\left[Ca^{2+}\right]_{nSR} - \left[Ca^{2+}\right]_{jSR} \end{array} \right)\tau_{jSR}^{-1} \left. \begin{array}{c} \forall n \in \theta_{dyad}(m) \\ \\ \forall n \notin \theta_{dyad}(m) \end{array} \right\} \qquad (17)$$

3 Where all dyad-specific dynamics ($[Ca^{2+}]_{ds}$ and $[Ca^{2+}]_{jSR}$ terms) are solved only for voxels
4 containing dyads (note that the above ensures those which do not contain dyads have no
5 contribution from them). In the fully idealised models, these dyads can be evenly distributed
6 throughout the cell volume at intervals of 1-2 μm (Figure 2Bii), or according to randomly
7 produced distributions for theoretical study; the distances between dyads is necessarily limited
8 to the same discretisation as the chosen space step, Δx.

9 ### 3.3.2. Distributing membrane and SR fluxes

10 In fully idealised approaches, the sarcolemmal membrane (surface and TT) and SR occupy the
11 entire intracellular volume and are present in every voxel. However, this is not physiologically
12 representative nor a requirement of this approach: both may be restricted to a subset of the
13 intracellular voxels and thus have their own structure. The structures themselves can be derived
14 from experimental imaging data, as described later, or theoretically generated "cartoon"
15 geometries. Dependent on the available data and desires, some or all of the following
16 considerations can be included: (i) non-idealised dyad distribution and heterogeneous RyR and
17 LTCC channel numbers; (ii) structure of the surface sarcolemma and T-system; (iii) structure
18 of the SR; (iv) relative expression of sarcolemmal and/or SR channels along these membranes.

19 Distributing dyads according to different spatial geometries involves defining the mapping
20 functions to correctly relate dyads to voxels. Similar mapping functions can also be used to
21 localise and distribute the membrane and SR fluxes according to the desired structure. Thus,
22 we introduce the membrane maps ($\theta_{mem}(p) = n;\ \theta_{mem}^{-1}(n) = p$) and SR maps ($\theta_{SR}(q) = n;\ \theta_{SR}^{-1}(n) = q$) which relate membrane and SR voxels ($p = 1, 2 \ldots P;\ q = 1, 2 \ldots Q$) to the intracellular
23
24 space voxel. Note that under these additions, the model is no-longer a homogeneous tri-domain
25 model, as not every voxel necessarily contains a network SR domain. Thus, the reaction term
26 for the cytoplasm (equation 9) and SR (equation 10) are updated accordingly:

27
$$^{n}\phi_{i} = \left. \begin{array}{c} -{}^{n}J_{trpn} \\ \\ ^{\theta_{mem}^{-1}(n)=p}J_{NaCa} + {}^{p}J_{pCa} + {}^{p}J_{Cab} - {}^{n}J_{trpn} \\ \\ -\left(^{\theta_{SR}^{-1}(n)=q}J_{up} - {}^{q}J_{leak} \right) - {}^{n}J_{trpn} \\ \\ ^{\theta_{mem}^{-1}(n)=p}J_{NaCa} + {}^{p}J_{pCa} + {}^{p}J_{Cab} - \left(^{\theta_{SR}^{-1}(n)=q}J_{up} - {}^{q}J_{leak} \right) - {}^{n}J_{trpn} \end{array} \right\} \begin{array}{l} \forall n \notin \theta_{mem}(p) \wedge \notin \theta_{SR}(q) \\ \\ \forall n \in \theta_{mem}(p) \wedge \notin \theta_{SR}(q) \\ \\ \forall n \notin \theta_{mem}(p) \wedge \in \theta_{SR}(q) \\ \\ \forall n \in \theta_{mem}(p) \wedge \in \theta_{SR}(q) \end{array}$$

28
$$(18)$$

29
$$^{\theta_{SR}^{-1}(n)=q}\phi_{nSR} = \left({}^{q}J_{up} - {}^{q}J_{leak} \right)\left(v_{i}/v_{nsr} \right) \left. \begin{array}{c} \forall n \in \theta_{SR}(q) \\ \\ \forall n \notin \theta_{SR}(q) \end{array} \right\} \qquad (19)$$

Where $^qJ_{up}$, $^qJ_{leak} = f(^{\theta_{SR(q)=n}}[Ca^{2+}]_{cyto}, ^q[Ca^{2+}]_{SR,})$. For any structures considered idealised (occupying the entire intracellular volume) there is therefore a one-to-one mapping with the intracellular space, and the general form of the equation is restored.

3.4. Heterogeneous ion channel expression in the sub-cellular volume

Heterogeneous expression of the flux channels can be incorporated by scaling the local maximal flux rates and/or channel numbers around the mean while maintaining total channel expression. For the membrane fluxes this gives:

$$^pJ_X = {}^pG_X.J_X^{max}.f(^{\theta_{mem(p)=n}}[Ca^{2+}]_{cyto},V_m)$$

$$\sum_{p=1}^{p=P}\left(\frac{^pG_X}{P}\right)=1 \tag{20}$$

Where X represents any of the membrane fluxes in equation 9. Similarly, for the SR fluxes (J_{up} and J_{leak}):

$$^qJ_X = {}^qG_X.J_X^{max}.f(^{\theta_{SR(q)=n}}[Ca^{2+}]_{cyto},{}^q[Ca^{2+}]_{SR})$$

$$\sum_{q=1}^{q=Q}\left(\frac{^qG_X}{Q}\right)=1 \tag{21}$$

This approach can be equally applied to both compartmentalised and free-diffusion models.

4. Image-based modelling approaches

This section outlines approaches for modelling controllable and experimentally-matched heterogeneous structures in both types of spatial cell model. These approaches can be applied in future studies to help to rigorously establish the link between structure and emergent function in both physiological and pathophysiological conditions.

4.1. Direct image-based modelling using the free-diffusion models

The free-diffusion model developed in Colman et al. 2017 [12] and described above was specifically designed for the ability to directly include experimental reconstructions of the sub-cellular membrane structures and channel distribution, permitting *in silico* functional assessment of specific cellular structure. This section outlines the approaches for processing and discretising high-resolution cellular structural data for simulations; the reader is referred to the original paper for further details. The experimental imaging approaches to acquire these structural data are described elsewhere [24–26].

The model setup already includes the functionality for the sarcolemmal and SR membranes to contain their own structure within the intracellular volume. Thus, all that is required is to create the mapping functions which relate the dyad, membrane and SR voxels to intracellular voxels. The first step is to segment the desired structures from the imaging data (Figure 3A) based on user-determined thresholds – the desired output is binary: 1 representing the presence of the structure, 0 representing its absence.

The dyads in the model should be point-sources occupying one voxel each, and so down-sampling imaging data to the model discretisation should be relatively simple (Figure 3B). The T-tubules and SR should be continuously connected networks; smoothing of the data may be required to achieve this. For the T-tubules, the structure may be crudely down-sampled either using an image-processing tool, or using an explicitly defined threshold for the number of high-resolution voxels which correspond to its presence at low resolution. The process is more

7

complex for the SR, as the down-sampled resolutions may significantly obscure the network structure of the system (Figure 3C). Thus, rather than simple down-sampling, the network is first skeletonised and the connections along the network are mapped. The skeleton can then be down-sampled, with the connection map imposed to ensure new connections are not created through this down-sampling (Figure 3D).

Once we have structures which represent the T-system and SR at the spatial resolution of the model's intracellular space, sequentially numbering each element of the geometries allows a simple mapping of voxel n to structure map p, q. The fluxes interacting with the cytoplasm are thusly localised to these structures; diffusion of Ca^{2+} in the SR is solved using the connection map as a pseudo-1D cable.

If data on channel expression along the membranes are available, then the local flux at each map element can be scaled according to this relative expression data. The relative expression should be normalised to meet the constraint that the average is 1 (i.e. whole-cell channel expression is unaffected) and then this relative expression map defines local $^{p,q}G_x$ in equations 20-21.

4.2. Image-based modelling using the compartmentalised models

Despite the clear value of the structurally detailed free-diffusion models for investigations of heterogeneous sub-cellular structure, they are computationally intensive and restricted to the structural data available or cartoon geometries. The compartmentalised models can also be used for structurally heterogeneous investigation in a more systematic and general approach. The range of heterogeneities investigated is more limited than the free-diffusion model (for example, inter-dyad distance and co-localisation distances are fixed in the current setup of the model), but can include: numbers of RyRs/LTCCs in each dyad, and the respective dyad and jSR volumes; the relative expression of all other Ca^{2+}-flux carrying channels in each CRU. These heterogeneities can be included by producing 3D maps which scale flux strength (or any other) parameters in individual CRUs relative to the global value, e.g. by directly setting the local flux scale-factor $^{p,q}G_x$. This section will first discuss methods for producing spatially correlated relative expression maps, followed by methods for analysing real imaging data to perform image-based modelling using these idealised models.

4.2.1. Modelling spatially heterogeneous channel expression

A crude approach to modelling sub-cellular heterogeneity in channel expression could be simply to use a random number generator to produce a randomly populated scaling map, imposing a selected probability density function. However, a spatial random field can also be used which accounts for the spatial correlation in channel expression, ensuring the expression in one CRU is not independent of that in its neighbour. A random field, $F(x)$, is a random function over some arbitrary (usually multi-dimensional) system, which can be described as a set of continuous indexed variables $x \in \Omega$, where Ω is an open set of $\mathbb{R}^d$ which describe the geometry of the system [27,28]. The main statistics of random fields are the mean, variance and correlation length (length scale), which can have their own functions.

One class of correlated random field is a Gaussian random field (GRF) which uses the Gaussian probability density function with an exponential covariance (a 1-D GRF is also called a Gaussian Process) [29]. Through applying Gaussian functions to these statistics, the random field can be constrained, allowing 3D heterogeneous expression maps (Figure 4A) to be produced with given spatial parameters. The length-scale, λ, determines the spatial extent of correlated expression: at the CRU resolution (i.e. 1μm) this is equivalent to a spatially uncorrelated map; as length scale increases, the rate of spatial variation decreases (Figure 4B). Anisotropic maps can also be produced wherein the length scales in the transverse and longitudinal directions are not equal (i.e. $\lambda_T \neq \lambda_L$; Figure 4B), which may be more

representative of cardiac sub-cellular structure. It is vital to impose the constraint when producing these maps that the mean scale factor remains 1, such that the inclusion of such heterogeneity does not affect whole-cell expression.

The impact of such sub-cellular heterogeneity on the spatial and average properties of the Ca^{2+} transient can be substantial, in particular when heterogeneity in multiple targets (e.g. SERCA and RyR) are considered in combination (Figure 4C). Preliminary simulations indicate such heterogeneities may be linked to both Ca^{2+}-transient alternans and spontaneous excitation. For those interested in exploring this further, we have developed user-friendly tools to generate these maps, suitable for use in our simulation framework, which can be found in the "Sub_cellular_heterogeneity_TOOLKIT" repository on the lab's Github.

4.2.2. Methods for data processing for image-based modelling

This section discusses processing cellular imaging datasets in order to extract the information necessary to generate spatial maps which are congruent with the experimentally measured properties. In brief, we want to extract the length scales in the transverse and longitudinal directions which may be used as inputs to generate sets of randomly produced maps with those properties. A variogram model is used to estimate these length scales from the microscopy data.

Extracting the variation parameters from microscopy data required the construction of a semi-automatic pipeline which processes the image data into a suitable format for analysis, and a method of fitting the processed data to some spatial covariance function which includes a description of correlation length scales. This semi-automatic pipeline is available in the "Sub_cellular_heterogeneity_TOOLKIT" repository on the lab's Github, which contains worked examples for data processing. The process of this analysis is described below.

The processed dataset must contain a suitably large quantity of data in order to obtain meaningful values of longitudinal and transversal length scales. The image data should be rotated such that the longitudinal and transversal axes are in alignment with the x and y axes of the image (Figure 5A). Rotated images are then cropped and down-sampled to a resolution of 1-2 μm (Figure 5A). This down-sampling is essential for length-scale analysis, as we require a continuous distribution representing the average relative expression of each channel per CRU, suitable for comparing different CRUs, and therefore need to remove the internal underlying membrane structure; the down-sampled image should be suitable for visualisaton as a contour map (Figure 5A). The variogram fitting procedure can then be applied to obtain the relevant parameters corresponding to that slice (Figure 5A). The process is repeated for all suitable x-y slices in the z-stack of images, and the summary parameters for the whole-cell can be obtained. These parameters can then be used to generate sets of 3D heterogeneity maps for use in simulations (Figure 5B).

5. Methods for multi-scale investigation of spontaneous calcium release

Multi-scale investigation of spontaneous Ca^{2+} release events (SCRE) is one of the major motivations for developing such detailed models of spatio-temporal Ca^{2+} handling. The challenge is that the spatial models discussed above are unsuitable for tissue-scale simulations, whereas efficient point-source cell models cannot reproduce stochastically induced SCRE. In parallel with the pioneering work of [18,19,30,31], an independent novel approach was developed to accurately reproduce the statistics and dynamics of SCRE in efficient cell models suitable for tissue simulations [11,13,32]. Described in detail in Colman 2019 [13], this involved the introduction of spontaneous release functions (SRF): analytical waveforms describing RyR open state occupancy with controllable parameters to match the timing,

1 amplitude and duration of SCRE observed in the spatial cell models and/or experiments. These
2 functions, and algorithms to implement them with dynamic cell models, are packaged with the
3 MSCSF on the lab's Github.

4 5.1. The Spontaneous Release Functions

5 The SRF aim to capture the temporal evolution of the open RyR waveform associated with
6 SCRE, based on simulated SCRE emerging from the compartmentalised 3D cell model (Figure
7 6A). Waveforms occur in broadly two forms: long-duration, spike-and-plateau like (e.g. at low
8 Ca^{2+} load), and short-duration spike-like (e.g. at high Ca^{2+} load; Figure 6A). The primary
9 properties of these waveforms which need to be reproduced are: (1) the initiation time, t_i,
10 referring to the time of onset of SCRE; (2) the duration of the waveform; and (3) the amplitude.
11 These parameters can be used to define SRF which approximate this temporal evolution:

$$12 \qquad N_{RyR\_O} = N_{RyR\_O}^{peak}\left[\left(1+e^{-(t-t_1)/k_1}\right)\left(1+e^{-(t-t_2)/k_2}\right)\right]^{-1} \tag{22}$$

$$13 \qquad t_1 = t_i + 0.5\left(t_p - t_i\right) \tag{23}$$

$$14 \qquad t_2 = t_p + 0.5\left(t_f - t_p\right) \tag{24}$$

$$15 \qquad k_1 = 0.1689(t_p - t_i) + 0.00255 \tag{25}$$

$$16 \qquad k_2 = 0.1689\left(t_f - t_p\right) + 0.00255 \tag{26}$$

17 where t_i is the initiation time of the SCRE, t_f is the end time (duration, λ, thus $= t_f\text{-}t_i$), t_p is the
18 time of the peak of the waveform and $N_{RyR\_O}^{peak}$ is the peak of open proportion RyR (Figure
19 3D). The constants in equations (25,26) were obtained from best fits to the waveforms
20 observed. The function for the plateau-like waveform (corresponding to durations longer than
21 300 ms) is derived from the same parameters:

$$22 \qquad N_{RyR\_O} = \begin{aligned} &N_{RyR\_O}^{plateau}\left[\left(1+e^{-(t-(t_i+17.5))/5.946}\right)\left(1+e^{(t-(t_f-17.5))/5.946}\right)\right]^{-1} + \\ &\left(N_{RyR\_O}^{peak} - N_{RyR\_O}^{plateau}\right)\left[\left(1+e^{-(t-(t_p-25))/5.946}\right)\left(1+e^{(t-(t_p+17.5))/5.946}\right)\right]^{-1}\end{aligned} \tag{27}$$

23 Where $N_{RyR\_O}^{plateau}$ is the amplitude of the plateau.

24 Due to the stochastic nature of SCRE, these properties are all variable and described by
25 distributions (Figure 6B). In order to appropriately determine individual waveform parameters,
26 these can be randomly sampled from the defined distributions.

27 (1) - t_i: The probability density functions for the initiation time do not demonstrate a normal
28 distribution, but rather a skewed distribution. The cumulative frequency is well approximated
29 by the use of two simple sigmoidal functions (Figure 6B):

$$30 \qquad F(t_i) = \begin{aligned}\begin{cases} F_1(t_i) = \left(2CF_{t_{i,Sep}}\right)\left(1+e^{-(t_i-t_{i,sep})/k_{F_1}}\right)^{-1} & t_i < t_{i,Sep} \\ F_2(t_i) = \left(2\left(1-CF_{t_{i,Sep}}\right)\right)\left(1+e^{-(t_i-t_{i,sep})/k_{F_2}}\right)^{-1} -1+2CF_{t_{i,Sep}} & t_i \geq t_{i,Sep}\end{cases}\end{aligned} \tag{28}$$

1   The distribution for t_i is therefore determined by four parameters: the initiation time
2   corresponding to the point where the functions are separated ($t_{i,Sep}$); the cumulative frequency
3   at this point ($CF_{ti,Sep} = F(t_i)|_{ti=ti,Sep}$), and the gradient parameter of each function (k_{F1}, k_{F2} -
4   corresponding to the width of the distribution either side of $t_{i,Sep}$).

5   (2) $- \lambda$: The distributions for the duration are also non-normal, and well approximated by two
6   sigmoidal functions describing the cumulative frequency for half of the data either side of the
7   median duration (MD):

$$F(MD) = \begin{matrix} F_{D1}(MD) = \left(1 + e^{-(\lambda - MD)/0.261 DW_1}\right)^{-1} \\ F_{D2}(MD) = \left(1 + e^{-(\lambda - MD)/0.261 DW_2}\right)^{-1} \end{matrix} \left.\begin{matrix} \\ \\ \end{matrix}\right| \begin{matrix} \lambda < MD \\ \lambda \geq MD \end{matrix} \tag{29}$$

9   Where the widths (DW_1, DW_2, in ms) are a function of the MD, given by:

$$DW_1 = A_{DW1}\left(1 + e^{-(MD - a_{DW1})/k_{DW1}}\right)^{-1} + DW_1^{\min} \tag{30}$$

$$DW_2 = A_{DW2}\left(1 + e^{-(MD - a_{DW2})/k_{DW2}}\right)^{-1} + DW_2^{\min} \tag{31}$$

12   The duration distribution is therefore completely described by the median, MD. Note that the
13   widths (DW_1, DW_2) could also be specified directly for complete control over the variability in
14   duration. Within this, the timing of the peak, t_p, varies approximately evenly, occurring between
15   25 ms after the initiation (t_i) and 52 ms before the final time (t_f).

16   (3) - $N_{RyR\_O}^{peak}$; $N_{RyR\_O}^{plateau}$: The amplitude correlates strongly with duration, λ:

$$\left\langle N_{RyR\_O}^{peak} \right\rangle = 692.99 \lambda^{-1.6} + 0.059 \tag{32}$$

$$\left\langle N_{RyR\_O}^{plateau} \right\rangle = 31.09 (0.01\lambda)^{-7.39} + 0.034 \ \Big\} \ if \ \lambda > 300 ms \tag{33}$$

19   Full equations and parameters are presented in the Supplementary Material S2 – Model
20   description. With this setup, therefore, all parameters of the waveform are derived from two
21   primary waveform properties: the initiation time, t_i, and the duration, λ, which also determine
22   the peak time and amplitude; the distributions describing the variability of these properties is
23   entirely described by 5-7 parameters ($t_i = f(t_{i\_sep}, CF_{ti\_sep}, k_{F1}, k_{F2})$; $\lambda = f(MD, DW_1, DW_2)$ where
24   DW_1, $DW_2 = f(MD)$ or specified). Directly, these parameters can be defined by the user to
25   investigate the impact of these distributions on cellular SCRE and its manifestation in tissue.
26   A worked example, introducing a pathophysiological model and deriving the resulting SRF, is
27   provided in Supplementary Material S1 – Worked Examples.

28   It is also valuable to be able to determine these distribution parameters dynamically during a
29   simulation, based on the environmental variable of the SR - Ca^{2+} load. Specific approximations
30   can be performed to match the behaviour of the cell models under different conditions (Figure
31   6C). Moreover, a general and controllable approach was developed to facilitate systematic
32   analysis in the wide parameter space: The SR dependence of these distribution parameters can
33   be defined by functions of SR-Ca^{2+} load and user-defined parameters, offering full control of
34   SCRE dynamics (Figure 6C):

$$CaSR_{\min} = CaSR_{threshold} - 0.5 CaSR_{P\_range} \tag{34}$$

$$P(SCR) = f_1\left([Ca^{2+}]_{SR}\right) = \left[1 + \exp\left(-([Ca^{2+}]_{SR} - CaSR_{threshold})/0.1CaSR_{P\_range}\right)\right]^{-1} \quad (35)$$

$$t_{i\_Sep} = f_2\left([Ca^{2+}]_{SR}\right) = \left(t_{i,Sep}^{max} - t_{i,Sep}^{min}\right)e^{\left(-5\left([Ca^{2+}]_{SR} - CaSR_{min}\right)/\left(CaSR_{max} - CaSR_{min}\right)\right)} + t_{i,Sep}^{min} \quad (36)$$

$$MD = f_3\left([Ca^{2+}]_{SR}\right) = \left(MD^{max} - MD^{min}\right)e^{\left(-5\left([Ca^{2+}]_{SR} - CaSR_{min}\right)/\left(CaSR_{max} - CaSR_{min}\right)\right)} + MD^{min} \quad (37)$$

$$k_{F_1} = f_1\left(t_{i,Sep}\right) = 0.145\left[\left(t_{i,width}^{max} - t_{i,width}^{min}\right)\left[\left(t_{t,Sep} - t_{i,Sep}^{min}\right)/\left(t_{i,Sep}^{max} - t_{i,Sep}^{min}\right)\right]^{H_{width}} + t_{i,width}^{min}\right] \quad (38)$$

$$k_{F2} = 1.5k_{F1} \quad (39)$$

$$DW_1 = f_1\left(MD\right) = \left(\lambda_{width}^{max} - \lambda_{width}^{min}\right)\left[\left(MD - MD^{min}\right)/\left(MD^{max} - MD^{min}\right)\right]^{H_{width}} + \lambda_{width}^{min} \quad (40)$$

$$DW_2 = DW_1 \quad (41)$$

Where the user-defined parameters refer to: The threshold for SCRE ($CaSR_{threshold}$); The SR-Ca^{2+} range over which $P(SCR)$ varies from 0 to 1 ($CaSR_{P\_range}$); The maximal SR-Ca^{2+} above which SCRE distributions converge ($CaSR_{max} > CaSR_{threshold} + CaSR_{P\_range}$); The minimum and maximum $t_{i,Sep}$ and MD ($t_{i,Sep}^{min}$, $t_{i,Sep}^{max}$, MD^{min}, MD^{max}); The t_i and λ distribution widths at these extremes ($t_{i,width}^{min}$, $t_{i,width}^{max}$, λ_{width}^{min}, λ_{width}^{max}); And the non-linearity of width variance (H_{width}).

The framework therefore uses the detailed, spatial cell models to derive the form of these SRF (Figure 6A-B); user inputs and/or SR-Ca^{2+} load are then used to define the distributions (Figure 6C), from which SRF parameters are randomly sampled to define individual waves (Figure 6D); these can then be integrated with non-spatial cell models, suitable for simulation in tissue (Figure 6E). This approach provides the means to investigate the mechanisms of synchronisation and dynamic interactions with tissue structure and arrhythmia conduction patterns such as re-entry [13].

6. Summary and conclusions

In this article, we have outlined methods for modelling sub-cellular spatial Ca^{2+} dynamics in cardiac cells, from the super-resolution through whole-cell up to the whole-heart scales. Such models are a powerful tool to investigate the multi-scale mechanisms underlying normal and abnormal cellular ECC as well as the emergence of Ca^{2+}-dependent arrhythmia.

7. Funding

8. Supporting information

All of the tools discussed in this article are available from the repository (https://github.com/michaelcolman/).

Worked examples are provided in the Supplementary Material S1 – Worked Examples.

Full model equations are provided in the Supplementary Material S2 – Model Description.

9. References

1. Eisner DA, Caldwell JL, Kistamás K, Trafford AW. Calcium and Excitation-Contraction Coupling in the Heart. Circ Res. 2017 Jul 7;121(2):181–95.

2. Eisner DA, Kashimura T, Venetucci LA, Trafford AW. From the ryanodine receptor to cardiac arrhythmias. Circ J Off J Jpn Circ Soc. 2009 Sep;73(9):1561–7.

3. Nattel S, Dobrev D. The multidimensional role of calcium in atrial fibrillation pathophysiology: mechanistic insights and therapeutic opportunities. Eur Heart J. 2012 Aug;33(15):1870–7.

4. Levy D, Kenchaiah S, Larson MG, Benjamin EJ, Kupka MJ, Ho KKL, et al. Long-term trends in the incidence of and survival with heart failure. N Engl J Med. 2002 Oct 31;347(18):1397–402.

5. Ceornodolea AD, Bal R, Severens JL. Epidemiology and Management of Atrial Fibrillation and Stroke: Review of Data from Four European Countries. Stroke Res Treat. 2017;2017:8593207.

6. Trayanova NA, Chang KC. How computer simulations of the human heart can improve anti-arrhythmia therapy. J Physiol. 2016;594(9):2483–502.

7. Vagos M, van Herck IGM, Sundnes J, Arevalo HJ, Edwards AG, Koivumäki JT. Computational Modeling of Electrophysiology and Pharmacotherapy of Atrial Fibrillation: Recent Advances and Future Challenges. Front Physiol [Internet]. 2018 [cited 2019 Jun 13];9. Available from: https://www.frontiersin.org/articles/10.3389/fphys.2018.01221/full

8. Restrepo JG, Weiss JN, Karma A. Calsequestrin-mediated mechanism for cellular calcium transient alternans. Biophys J. 2008 Oct;95(8):3767–89.

9. Li P, Wei W, Cai X, Soeller C, Cannell MB, Holden AV. Computational modelling of the initiation and development of spontaneous intracellular Ca2+ waves in ventricular myocytes. Philos Transact A Math Phys Eng Sci. 2010 Aug 28;368(1925):3953–65.

10. Song Z, Ko CY, Nivala M, Weiss JN, Qu Z. Calcium-voltage coupling in the genesis of early and delayed afterdepolarizations in cardiac myocytes. Biophys J. 2015 Apr 21;108(8):1908–21.

11. Colman MA, Perez Alday EA, Holden AV, Benson AP. Trigger vs. Substrate: Multi-Dimensional Modulation of QT-Prolongation Associated Arrhythmic Dynamics by a hERG Channel Activator. Front Physiol [Internet]. 2017 [cited 2018 Nov 29];8. Available from: https://www.frontiersin.org/articles/10.3389/fphys.2017.00757/full#B21

12. Colman MA, Pinali C, Trafford AW, Zhang H, Kitmitto A. A computational model of spatio-temporal cardiac intracellular calcium handling with realistic structure and spatial flux distribution from sarcoplasmic reticulum and t-tubule reconstructions. PLoS Comput Biol [Internet]. 2017 Aug 31 [cited 2019 Mar 4];13(8). Available from: https://www.ncbi.nlm.nih.gov/pmc/articles/PMC5597258/

13. Colman MA. Arrhythmia Mechanisms and Spontaneous Calcium Release: Bi-directional Coupling Between Re-entrant and Focal Excitation. PLOS Comput Biol. 2019;In press.

14. Gaur N, Rudy Y. Multiscale modeling of calcium cycling in cardiac ventricular myocyte: macroscopic consequences of microscopic dyadic function. Biophys J. 2011 Jun 22;100(12):2904–12.

15. Nivala M, Song Z, Weiss JN, Qu Z. T-tubule disruption promotes calcium alternans in failing ventricular myocytes: mechanistic insights from computational modeling. J Mol Cell Cardiol. 2015 Feb;79:32–41.

16. Song Z, Liu MB, Qu Z. Transverse tubular network structures in the genesis of intracellular calcium alternans and triggered activity in cardiac cells. J Mol Cell Cardiol. 2018 Jan;114:288–99.

17. Vierheller J, Neubert W, Falcke M, Gilbert SH, Chamakuri N. A multiscale computational model of spatially resolved calcium cycling in cardiac myocytes: from detailed cleft dynamics to the whole cell concentration profiles. Front Physiol [Internet]. 2015 [cited 2019 Jul 11];6. Available from: https://www.frontiersin.org/articles/10.3389/fphys.2015.00255/full

18. Campos FO, Shiferaw Y, Prassl AJ, Boyle PM, Vigmond EJ, Plank G. Stochastic spontaneous calcium release events trigger premature ventricular complexes by overcoming electrotonic load. Cardiovasc Res. 2015 Jul 1;107(1):175–83.

19. Campos FO, Shiferaw Y, Weber dos Santos R, Plank G, Bishop MJ. Microscopic Isthmuses and Fibrosis Within the Border Zone of Infarcted Hearts Promote Calcium-Mediated Ectopy and Conduction Block. Front Phys [Internet]. 2018 [cited 2019 Mar 13];6. Available from: https://www.frontiersin.org/articles/10.3389/fphy.2018.00057/full

20. Nivala M, de Lange E, Rovetti R, Qu Z. Computational Modeling and Numerical Methods for Spatiotemporal Calcium Cycling in Ventricular Myocytes. Front Physiol [Internet]. 2012 May 8 [cited 2020 Feb 10];3. Available from: https://www.ncbi.nlm.nih.gov/pmc/articles/PMC3346978/

21. Jayasinghe I, Clowsley AH, Lin R, Lutz T, Harrison C, Green E, et al. True Molecular Scale Visualization of Variable Clustering Properties of Ryanodine Receptors. Cell Rep. 2018 Jan 9;22(2):557–67.

22. Alvarez-Lacalle E, Echebarria B, Spalding J, Shiferaw Y. Calcium alternans is due to an order-disorder phase transition in cardiac cells. Phys Rev Lett. 2015 Mar 13;114(10):108101.

23. Rovetti R, Cui X, Garfinkel A, Weiss JN, Qu Z. Spark-induced sparks as a mechanism of intracellular calcium alternans in cardiac myocytes. Circ Res. 2010 May 28;106(10):1582–91.

24. Pinali C, Bennett H, Davenport JB, Trafford AW, Kitmitto A. Three-dimensional reconstruction of cardiac sarcoplasmic reticulum reveals a continuous network linking transverse-tubules: this organization is perturbed in heart failure. Circ Res. 2013 Nov 8;113(11):1219–30.

25. Jayasinghe I, Clowsley AH, Lin R, Lutz T, Harrison C, Green E, et al. True Molecular Scale Visualization of Variable Clustering Properties of Ryanodine Receptors. Cell Rep. 2018 09;22(2):557–67.

26. Jayasinghe I, Clowsley AH, de Langen O, Sali SS, Crossman DJ, Soeller C. Shining New Light on the Structural Determinants of Cardiac Couplon Function: Insights From Ten Years of Nanoscale Microscopy. Front Physiol [Internet]. 2018 [cited 2019 May 11];9. Available from: https://www.frontiersin.org/articles/10.3389/fphys.2018.01472/full

27. Arregui-Mena JD, Margetts L, Mummery PM. Practical Application of the Stochastic Finite Element Method. Arch Comput Methods Eng. 2016 Mar;23(1):171–90.

28. Sudret B. Stochastic Finite Element Methods and Reliability A State-of-the-Art Report. :189.

29. Clayton RH. Dispersion of Recovery and Vulnerability to Re-entry in a Model of Human Atrial Tissue With Simulated Diffuse and Focal Patterns of Fibrosis. Front Physiol [Internet]. 2018 [cited 2019 May 23];9. Available from: https://www.frontiersin.org/articles/10.3389/fphys.2018.01052/full

30. Xie Y, Sato D, Garfinkel A, Qu Z, Weiss JN. So little source, so much sink: requirements for afterdepolarizations to propagate in tissue. Biophys J. 2010 Sep 8;99(5):1408–15.

31. Liu MB, de Lange E, Garfinkel A, Weiss JN, Qu Z. Delayed afterdepolarizations generate both triggers and a vulnerable substrate promoting reentry in cardiac tissue. Heart Rhythm Off J Heart Rhythm Soc. 2015 Oct;12(10):2115–24.

32. Colman MA, Parra-Rojas C, Perez-Alday EA. From microscopic calcium sparks to the ECG: Model reduction approaches for multi-scale cardiac simulation. In: 2015 Computing in Cardiology Conference (CinC). 2015. p. 325–8.
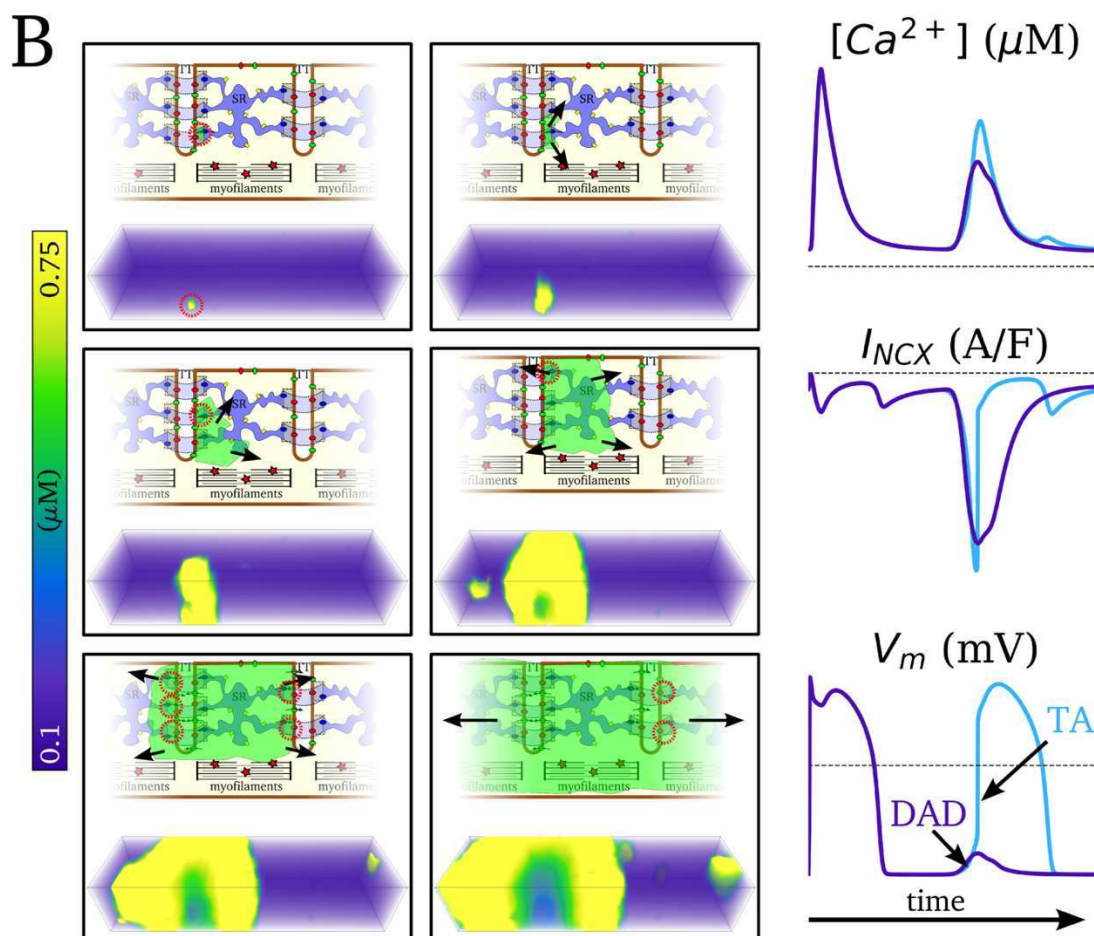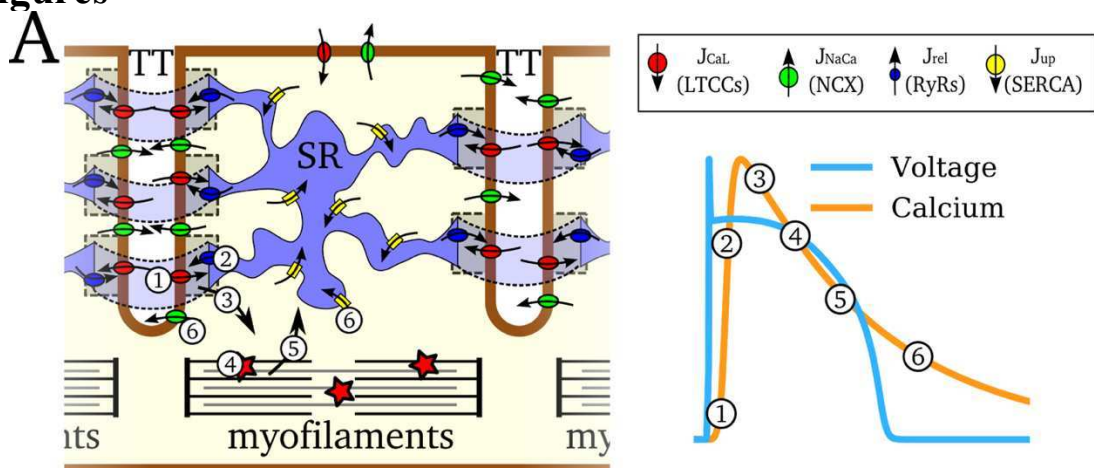
Figures

**Figure 1: Intracellular Ca²⁺ handling phenomena.** A − Schematic of the cardiac Ca²⁺ handling system (left) illustrating the phases of calcium-induced-calcium-release during electrical excitation, with the relationship between the AP and Ca²⁺ transient (right). The primary fluxes are illustrated with the coloured ovals and directional arrows, and the phases of CICR are labelled: 1) Ca²⁺ influx through the LTCCs during excitation; 2) Ca²⁺ release from the SR through the RyRs; 3) diffusion into the bulk intracellular space; 4) binding with the contractile proteins; 5) mechanical relaxation releases Ca²⁺ back into the bulk space; 6) refilling of the SR through SERCA and Ca²⁺-efflux through NCX. B − illustration of the mechanisms

16

of spontaneous excitation. The left panels show snapshots of calcium dynamics in the schematic (upper) and using simulated data (lower). In the upper panels, the green regions indicate high Ca^{2+} concentration and dyads undergoing Ca^{2+} release are circled in red dotted lines. Illustrated are: 1) spontaneous Ca^{2+} spark; 2) propagation in the transverse direction triggering more sparks; 3) propagation in the longitudinal direction, activating dyads on neighbouring T-tubules. The right panel shows examples of the Ca^{2+} concentration, I_{NCX} waveform and membrane potential associated with a stimulated excitation followed by a spontaneous Ca^{2+} release event, illustrating a case in which the DAD both does and does not manifest as a full triggered AP; the dotted line represents zero in y.
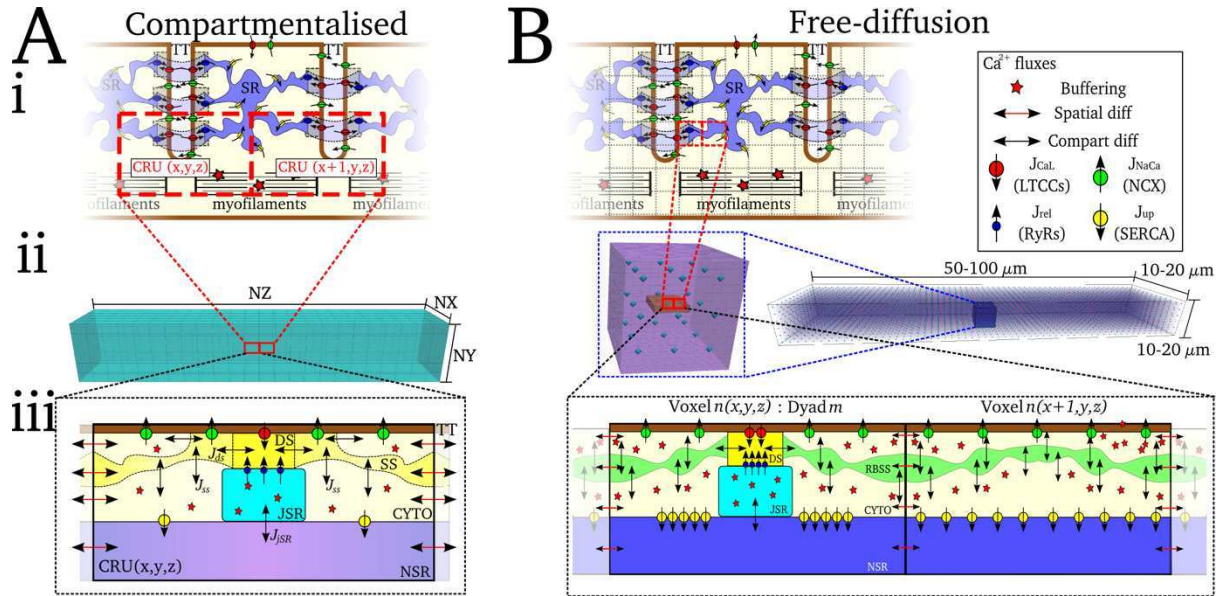
Figure 2: Schematics of the two different approaches for spatial cell modelling. A – the compartmentalised model involves coarse-graining the volumes associated with each dyad into a calcium-release-unit (i; CRU), which are arranged in a regular grid to form the cell (ii). The compartments of each CRU and the relevant fluxes and inter-compartment transfer are illustrated in (iii). Labelled are the dyadic cleft space (DS), sub-space (SS), bulk cytosolic space (CYTO), network and junctional SR spaces (NSR, JSR), and a T-tubule (TT). B – the free-diffusion model involves discretising the intracellular space as a free-diffusion volume (i), with voxels which both do and do not contain dyads; dyads are regularly distributed throughout the volume of the intracellular space (ii). The structure of each voxel is almost identical to that of a CRU (iii), with the exception of the presence or absence of dyads, TTs or the SR (according to the maps).
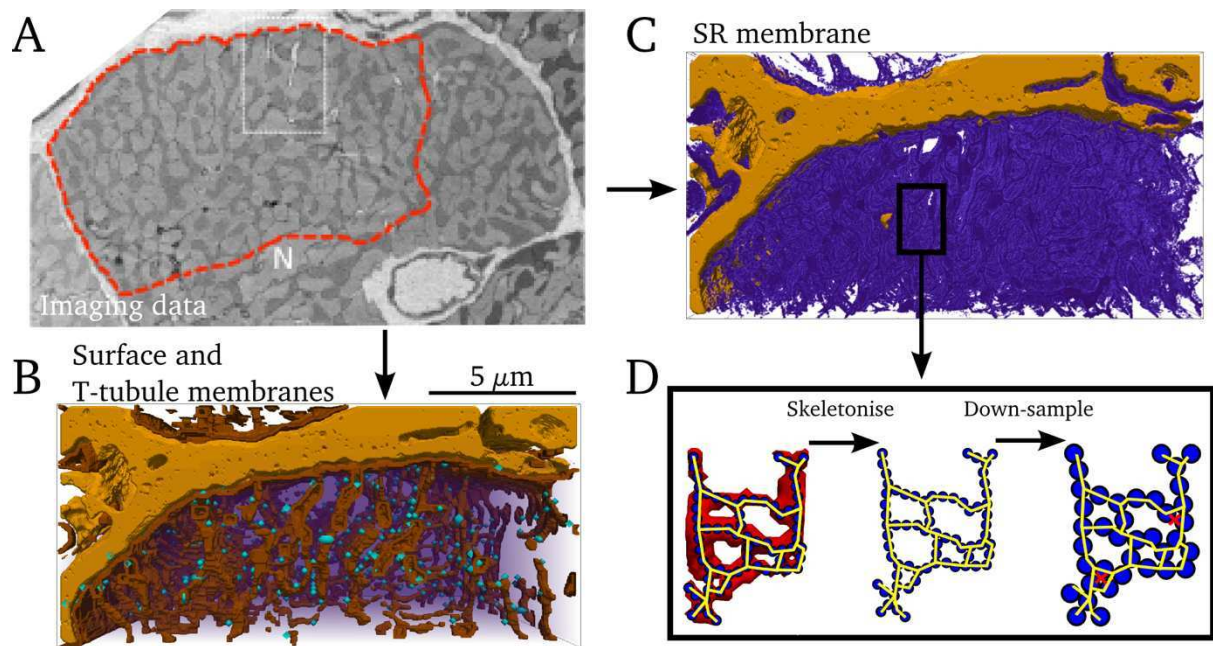
Figure 3: Processing structural data for direct image-based modelling. A – Example of a slice of electron-microscopy images of cardiac sub-cellular structure from which simulation geometries can be produced (data from [24] and image from [12]). B – Reconstruction of the surface sarcolemma (light brown), T-tubules (dark brown) and dyad locations (blue dots) within the intracellular space (purple volume). C – Reconstruction of the SR in 3D (purple) and method for down-sampling (D).

1
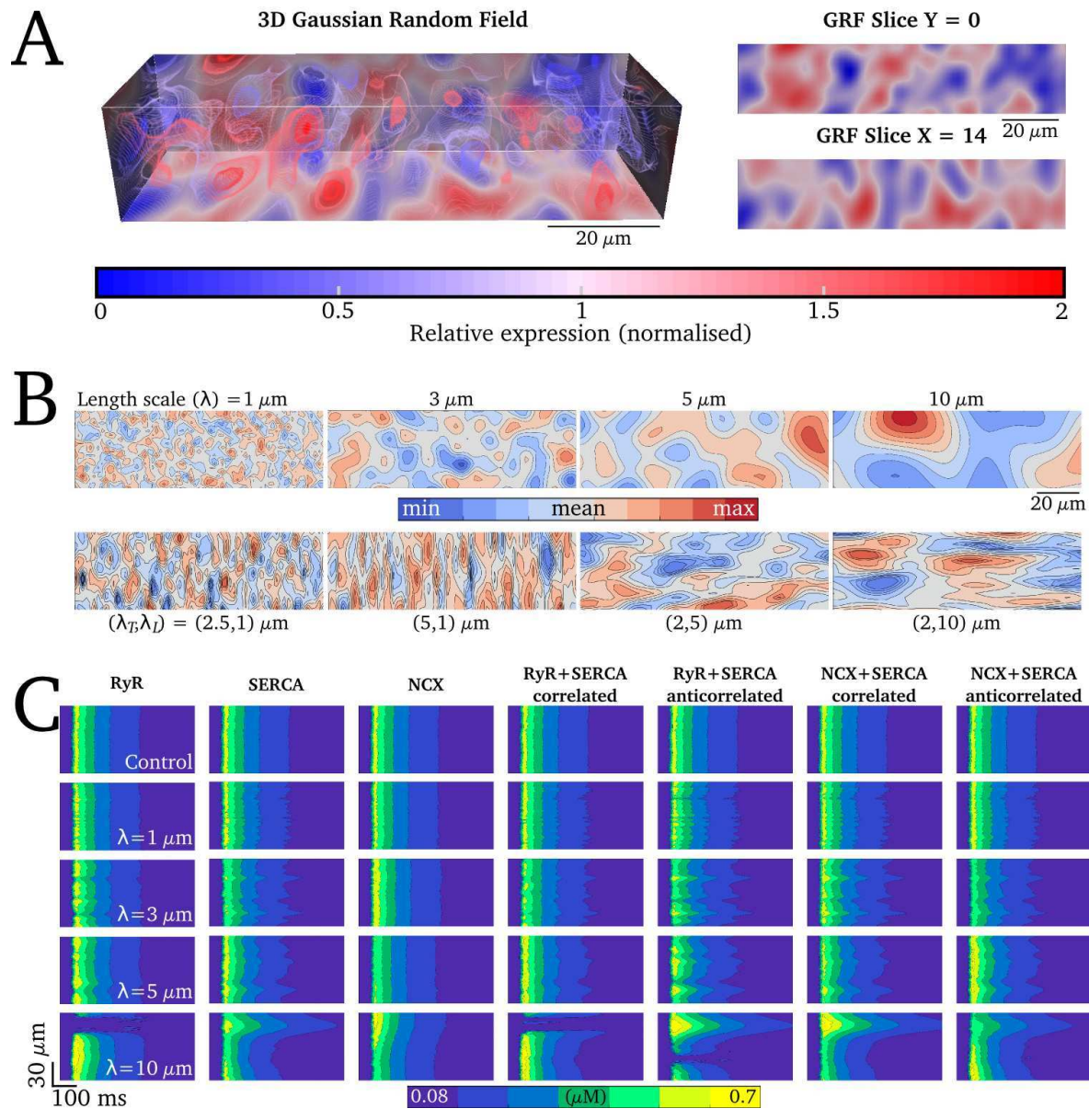
2
3
4 **Figure 4: Illustration of using spatial random fields to model sub-cellular channel**
5 **expression heterogeneity.** A – Example of a 3D GRF map, visualised using a contour plot
6 applied to 2D slices of the back surfaces, and semi-transparent contours throughout the volume;
7 two individual 2D slices are also shown for clarity. B – Example slices showing isotropic
8 (upper) and anisotropic (lower) GRF maps produced at different length scales and anisotropy
9 ratios. C – Examples of the influence of sub-cellular heterogeneity in RyR, SERCA and/or
10 NCX emerging from GRF maps with different length-scales. The plot visualises a linescan of
11 Ca^{2+} concentration along the longitudinal axis of the cell (y-axis) in time (x-axis).
12
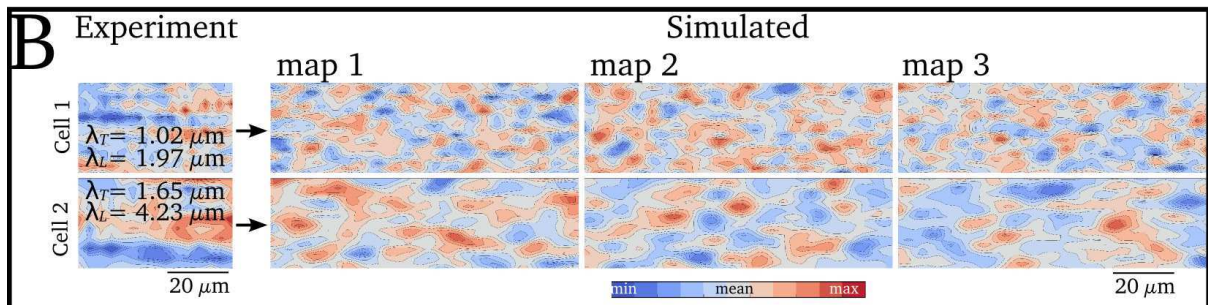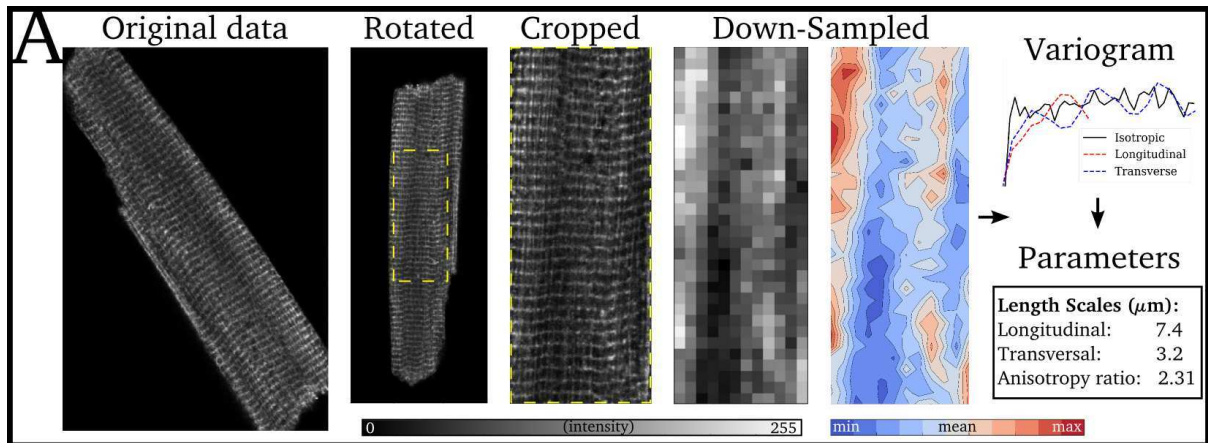
Figure 5: Image-based modelling using the compartmentalised models. A – Illustration of the processing required to extract length scales from cellular imaging data (in this example of SERCA expression). B – Examples of 2D slices from three independently produced GRF maps based on the parameters extracted from two different cells.
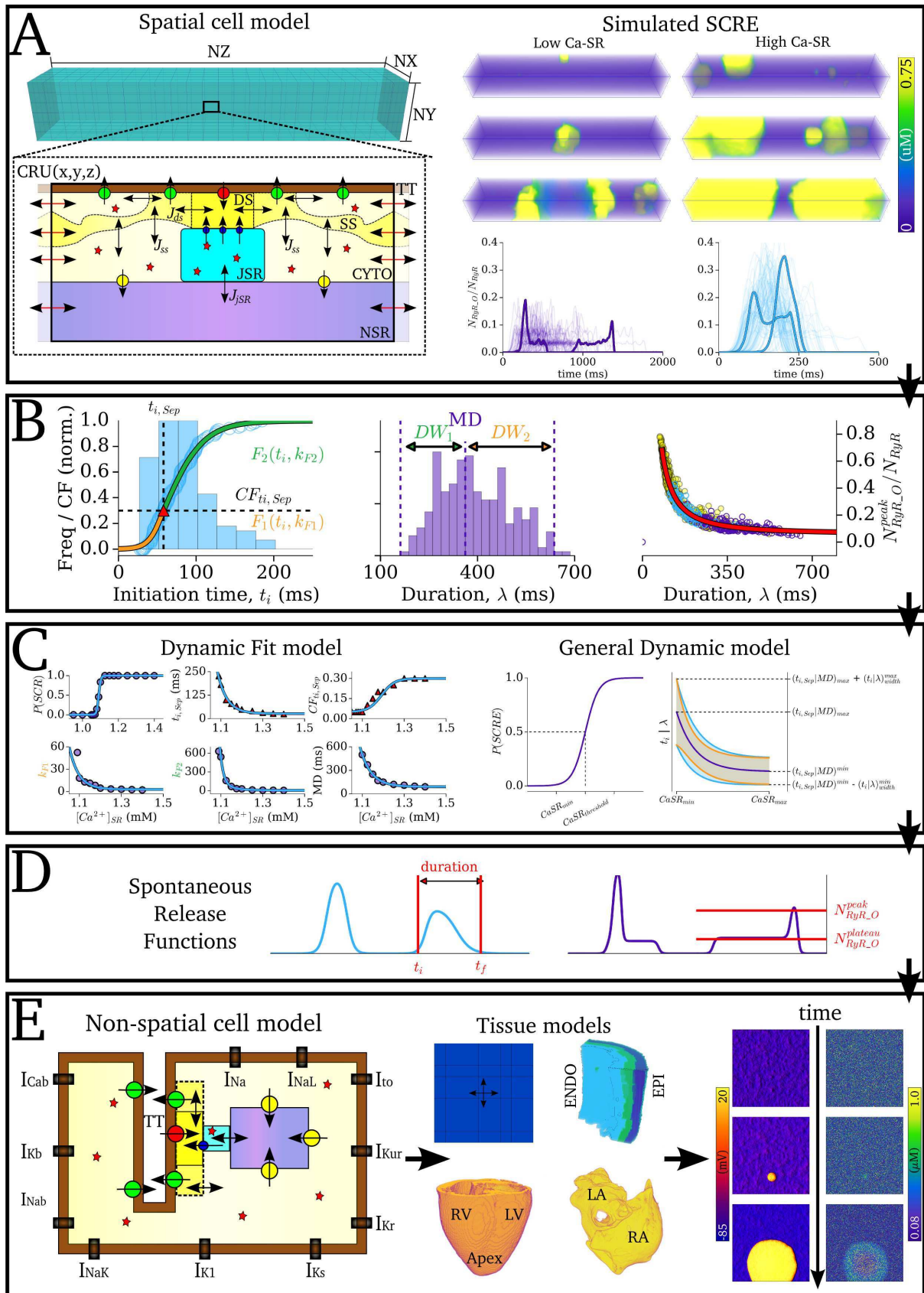
Figure 6: The computational framework for multi-scale simulation of spontaneous calcium release. A - 3D, microscopic Ca²⁺ handling model (left), illustrating the 3D grid of calcium release units (CRUs; upper panel) and the compartments and Ca²⁺ fluxes within a single CRU (lower panel). Labelled are the dyadic cleft space (DS), sub-space (SS), bulk

cytosolic space (CYTO), network and junctional SR spaces (NSR, JSR), and a T-tubule (TT); simulated SCRE (right) showing three snapshots of Ca^{2+} waves at low (left) and high (right) SR-Ca^{2+}; lower panels are overlays of 100 simulations at each SR-Ca^{2+}. B – Statistics of SCRE, showing the distributions associated with initiation time (left), duration (middle) and peak RyR (right). Examples of two functions – and their relevant parameters – to fit the cumulative frequency of initiation time are shown. C – Defining the distribution parameters based on SR-Ca^{2+}, illustrating the Dynamic Fit model (left) and General Dynamic model (right). D – Illustration of the analytical spontaneous release functions, defined by the parameters randomly sampled from the initiation time and duration distributions. Those illustrated correspond to the highlighted waveforms in A. E – Schematic of the non-spatial cell model (left), illustration of the tissue models (middle), and example simulation of a SCRE mediated focal excitation (right).